Simulated Data Sets for the Megamaser Cosmology Project

Jiwon (Jesse) Han

College of Arts and Sciences

University of Virginia

A thesis submitted for partial completion of the requirements of

B.S. Astronomy-Physics

May 2018

Abstract

The Megamaser Cosmology Project (MCP) is an NRAO Key Science Project to measure the Hubble Constant, H_0, by determining geometric distances to circumnuclear 22 GHz H_2O megamasers in galaxies well into the Hubble flow. Two independent measurements from VLBI mapping and single-dish spectral monitoring are fitted to a 3 dimensional thin disk model to determine the distance to the megamaser host galaxy. This thesis contributes to the MCP by simulating VLBI data sets through which numerous studies on systematic errors and optimizing observations can be accomplished. As a sample analysis, we investigate the relationship between the a priori uncertainties from the observations and the a posteriori distance uncertainty. In particular, we span the observational error space from $(\delta\nu, \delta A) = (0.2\text{mJy}, 0.05\text{km/s/yr})$ to $(2.0\text{mJy}, 0.25\text{km/s/yr})$, where $\delta\nu$ represents the VLBI mapping noise and δA is the uncertainty in acceleration. The nominal value $(\delta\nu, \delta A) = (1.5\text{mJy}, 0.2\text{km/s/yr})$ is accepted as the current position of the MCP in the error space; the simulated data set using this value yields a 14% a posteriori distance uncertainty. To achieve a 10% distance uncertainty instead, we conclude that an acceleration uncertainty improvement of 0.15 km/s/yr is needed from the current error values.

Contents

List of Figures

Chapter 1

Overview of the Megamaser Cosmology Project

The Megamaser Cosmology Project (MCP) aims to determine the Hubble constant (H_0), a measure of the rate of expansion of the universe, down to the few percent level to improve the extragalactic distance scale and to constrain the nature of dark energy. We achieve this goal by measuring distances to galaxies deep into the Hubble flow with a method that is independent of the cosmic distance ladder. Instead, the MCP searches for active galaxies that host 22 GHz H_2O megamasers in the accretion disk of the central black hole. The high rotational velocity of this disk generates three distinct groups of masers in blue shifted, red shifted, and systemic velocities, which allows us to determine the rotation curve of the disk and also the black hole mass. Combined with independent acceleration measurements of the systemic masers, these measurements yield the physical size of the disk, which can then be simply divided by its angular size to yield the distance. In this chapter, we motivate the MCP by introducing two scientific topics of interest: the Hubble constant and the M_{BH}—σ relation. Then, we proceed to describe the strategy of the MCP, and introduce the need for a simulated data set.

1.1 The Hubble Constant

Despite its self-evident significance in cosmology, the Hubble constant remains contested in its exact value. A recent measurement based on an updated cosmic distance ladder by Riess et al. [10] reports $H_0 = 73.24 \pm 1.74$ km/s/Mpc, which is at a 3.4σ tension with $H_0 = 67.31 \pm 0.96$ km/s/Mpc, a calculation based on Cosmic Microwave Background (CMB) measurements by the Planck Collaboration [3] under the standard cosmological model. An independent analysis of three multiply imaged quasar systems with measured gravitational time delays yield $H_0 \cong 71.9 \pm 3$ km/s/Mpc [1]. Thus, the need for an H_0 measurement independent of the distance ladder or a cosmological model is now evident more than ever. This is precisely the goal of the MCP. While the exact measurement strategy of the MCP will be further discussed in section 1.3, the single-step estimation of extragalactic distances of the MCP provides an invaluable addition to the discussion on H_0. The MCP has so far determined $H_0 = 69.3 \pm 4.2$ km/s/Mpc from published observations of UGC 3789 [9], NGC 6264 [7], NGC 6323 [6], and NGC 5765b [4].

1.2 M_{BH}—σ Relations

Since the observation targets of the MCP consist of active galaxies and, specifically, their central supermassive black holes (SMBH), another scientific interest is the relation between SMBH masses and properties of the host galaxy. Such a relation provides insight into the co-evolution of SMBHs and their host galaxies. For example, Greene et al. [5] draws upon a wealth of black hole mass (M_{BH}) measurements based on megamaser observations to conclude that galaxy properties such as total stellar mass, central mass density, and central velocity dispersion are not correlated tightly with M_{BH}. Such a study is possible because the megamaser disks are well within the "gravitational sphere of influence," thus allowing the observer to directly probe the gravitational potential of the central black hole. Unlike distance measurements, which require independent acceleration measurements, the M_{BH} can be directly measured with high precision from the rotation curve alone.

1.3 Strategy of the MCP

The MCP fully exploits the detection of 22 GHz H_2O megamasers embedded in the accretion disks of AGN that are deep in the Hubble flow ($D > 50 Mpc$). Owing to their fantastic intensities, narrow linewidths ($\delta\nu \sim 2$km/s), and small angular size, these masers can be resolved from one another with VLBI. Since these masers are amplified within the disk material, maximum amplification occurs when the line of sight is aligned with the radius of the disk. This configuration is termed as "edge-on," while the orientation that is 90° offset is referred as "face-on." For an edge-on disk, as depicted in figure 1.2(a), the masers are grouped into blue shifted, red shifted, and systemic velocities, thus effectively delineating the rotation of the host accretion disk. Figure 1.1 provides an example spectrum of an edge-on galaxy, UGC 3789.

The distance to the galaxy is determined from two independent measurements from VLBI mapping and single-dish spectral monitoring. From the VLBI map, we can spatially resolve the masers to obtain the rotation curve of the accretion disk, which is Keplerian. From spectral monitoring, we obtain the acceleration in the line-of-sight velocity of the systemic masers. These two independent measurements are fed into a Markov Chain Monte Carlo (MCMC) fitting code that imposes a 3-dimensional thin disk model to the data. The disk model is described by 14 global parameters: the mass, velocity, and position of the black hole; the inclination and position angle of the disk with their respective first and second derivatives; the eccentricity of the disk; the angle of periastron and its first derivative; and the peculiar velocity.

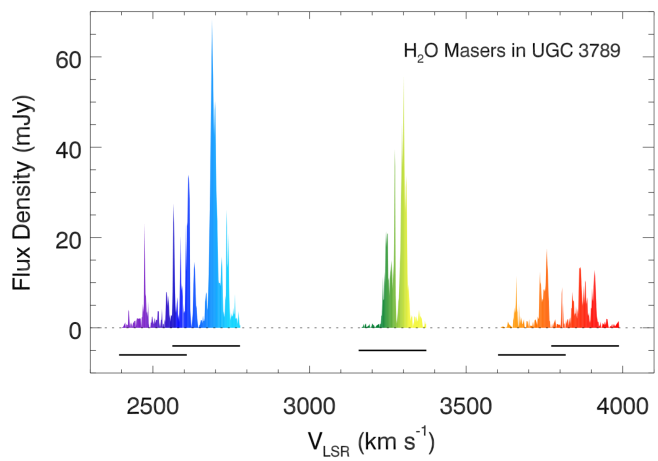

Figure 1.1: Triple-peaked velocity spectrum of UGC 3789 as presented in the first MCP paper [8].

1.4 Need for a Simulated Data Set

The challenge in determining the Hubble constant is mainly that of reducing systematic and random errors. The latter is obtained through many iterations of carefully planned observations. The former is a significant challenge, however, regardless of the measuring strategy. Simulated data can help to greatly improve and better understand systematic errors. By generating a synthetic data set and simulating its observation, we can accurately assess the robustness of the measuring strategy and also even discover unknown systematic errors that may have been glazed over by comparing the observed values with the exactly known generated values. Fortunately, the MCP is based on observations of systems with simple Keplerian dynamics that are relatively simple to simulate within some reasonable physical assumptions. Thus,

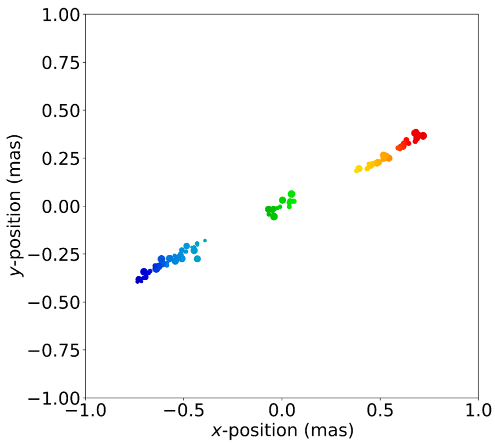

(a)

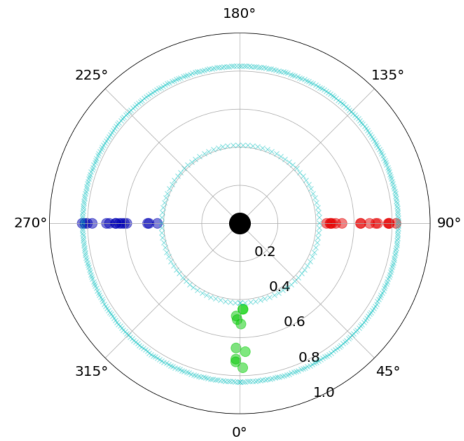

(b)

Figure 1.2: (a) Edge-on view of a maser galaxy with nonzero position angle. (b) Face-on view of a maser galaxy. Inner and outer radii marked light blue.

in this thesis, we simulate realistic observations motivated by physics, and thus provide the MCP collaboration with a means to assess systematic errors and to optimize obserations. The simulation process can be broken down into four stages as summarized in the flow chart in figure 1.3. An emphasis is made on constructing a modular structure so that individual pieces can be easily updated or modified. For example, we can probe the systematic errors that arise from different disk parametrization by simply modifying the disk generation module while fixing all other parts.

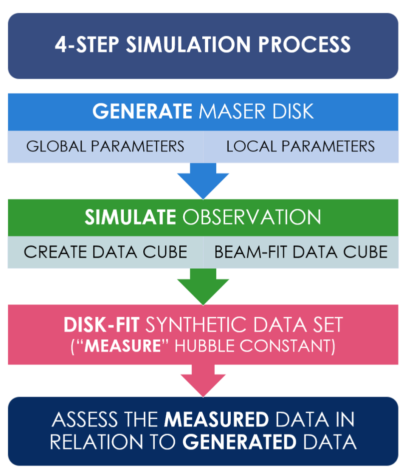

Figure 1.3: Workflow of simulating a data set.

Chapter 2

Simulating the Disk

There are three steps in simulating a realistic maser disk. The first step is to recreate the global dynamics of the accretion disk accurately. In particular, the rotation of the disk must be modeled to determine the line of sight velocities of the individual maser features. To first order, the gravitational potential of the central black hole dominates these velocities. Higher order effects from self-gravity, finite disk thickness, or relativity may also be introduced as perturbations on the order of a few percent. In this thesis, however, we keep such complications to minimum by assuming a thin disk[1] conforming to the Keplerian rotation curve defined by equation 2.1. Here, r_0 is the dynamic center of the black hole and r is the coordinate-free position vector.

$$v = \sqrt{\frac{GM}{|\mathbf{r} - \mathbf{r_0}|}} \tag{2.1}$$

The second step is to properly distribute the masers within the rotating disk. Under the assumption that the masers are scattered throughout the disk without a preferential azimuthal angle, the observer would detect masers distributed along the mid-line that is perpendicular to the line of sight, as illustrated in figure 1.2(a) and 1.2(b). As the final step, we assign observational properties to the masers. Specifically, the intensity and natural line width of each maser feature must be determined, since those two quantities are what we measure in an observation.

2.1 Global Parameters

The fundamental global parameters that generate the disk dynamics are the following: the black hole mass, the inner and outer radius of the maser disk, the position

[1]"Thin" does not exclude the possibility position angle and inclination angle warping.

and inclination angle of the disk, and the number of blue shifted, red shifted, and systemic maser features to be simulated. For the purpose of simulating a generic accretion disk, the poster child maser galaxy UGC 3789 provides a reference point for these parameters. Table 2.1 compares the parameters used in the simulated disk to that of UGC 3789.

Parameter	UGC 3789	Simulated Disk
M_{BH}	$1.16 \times 10^7 M_\odot$	$10^7 M_\odot$
Inner Radius	0.08 pc	0.1 pc
Outer Radius	0.30 pc	0.2 pc
Position Angle	221.5°	90°
Inclination Angle	90.6°	90°

Table 2.1: Global Parameters of UGC 3789 and the simulated disk.

2.2 Position Distribution

To best recreate the observed maser distribution, we explore a number of different regimes for the position distribution. For example, in the equidistant model, the masers are placed evenly throughout the disk, while in the clustering model, we generate clusters of masers throughout the disk within which masers are populated randomly. Throughout the rest of this thesis, a uniform random distribution is used to produce simulated data sets, while maintaining the interchangeability of the distribution scheme. In any given regime, an inner and outer radius is determined first to recreate the pronounced boundaries in the maser distribution observed in actual galaxies. In addition, we are also free to warp the inclination and position angle by defining their derivatives, as shown in figure 2.1(b).

2.3 Feature Assignment

For an unsaturated maser, the pumping process dominates losses from stimulated emission to maintain population inversion, generating an exponential amplification along the gain path. Thus, the slightest change in position can result in a stark contrast in amplitude; this results in a seemingly stochastic amplitude distribution. However, once the maser saturates, equilibrium population inversion is no longer maintained, and the amplification becomes linear with respect to the gain path and

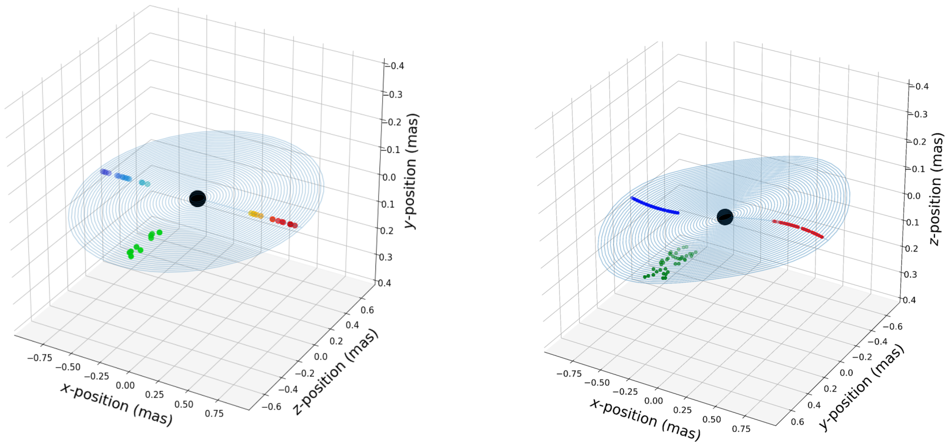

(a) (b)

Figure 2.1: (a) 3D map of a flat disk with distributed masers. (b) 3D map of a disk with finite position angle curvature.

population size. Thus, an amplitude envelope is set under which random fluctuations occur from unsaturated masers.

In the setting of an accretion disk, the maximum gain path is limited by velocity coherence along the line of sight due to the rotation. Assuming a Keplerian velocity profile, we can calculate this maximum gain path, $l(x)$, that preserves velocity coherence within the limits of Doppler broadening δ_v, as described in figure 2.2 and equation 2.2.

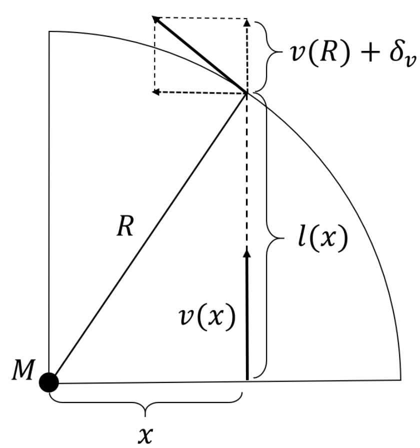

Figure 2.2: Maximum gain path dependence on impact parameter, x.

$$l(x) = \left[x \left(\frac{\delta_v}{GM} + \frac{1}{x} \right) - x^2 \right]^{1/2} \tag{2.2}$$

Under this envelope, we randomly sample the individual amplitudes from an exponential distribution. This choice also has the benefit that it recovers the pedestal-like structure around groups of maser features observed in real data. In addition, to match the observed spectra, we choose the natural line width to be 2 km/s. As a final step, the velocity for all of the simulated masers are adjusted for the recession velocity of the galaxy, which is calculated from the distance and Hubble constant. For the purpose of simulating a data set, we are free to simply set the Hubble constant to a nominal value, which can later provide a testament to the accuracy of the MCP fitting code.

Chapter 3

Generating the Data Cube

Any simulated physical object must be complemented by an accurate "observation." That is, the simulated data must be appropriately corrupted in a such a way that reflects a realistic observation. Thus, in this chapter, we emulate a VLBI observation of the simulated, idealized maser disk. The observation can be broken down into three steps. First, the simulated maser disk is converted into a signal data cube. In actual VLBI data, this cube consists of right ascension, declination, and velocity axes. Similarly, the data cube created here is assigned two position axes (x and y) and a velocity axis. Second, a noise cube is separately generated to represent beam-convolved Gaussian noise. By adding the signal cube to the noise cube, we obtain the data cube that is analogous to reduced data from a VLBI observation, which we will hereby refer to as the "science cube." The last step is then to glean the positionts of the observed maser features from the science cube. This is accomplished by applying a fitting code used in actual MCP observations to the science cube.

3.1 Creating the Signal Cube

The signal cube is generated by treating each maser as a perfect point source, convolved with the observing VLBI beam shape. In practice, this convolution amounts to assigning each simulated maser feature a 3 dimensional Gaussian function parametrized by the beam size and maser line width. Assuming that each axis is uncorrelated with another, this function takes the form of equation 3.1.

$$Ae^{-\left[\frac{(x-\mu_x)^2}{2b_x^2}+\frac{(y-\mu_y)^2}{2b_y^2}+\frac{(v-\mu_v)^2}{2\sigma_v^2}\right]} \tag{3.1}$$

Here, μ_x and μ_y are respectively the simulated positions of the maser, while b_x and b_y are the respective beam size in each axis. In general, the beam shape is elliptical due to the asymmetric distribution of VLBI antennae that are scattered longer in the East-West direction than North-South. To incorporate this asymmetry, b_y is set to be three times wider than b_x. Next, μ_v is the simulated line-of-sight velocity of the maser, while σ_v is the natural line width of the maser. A corresponds to the physical intensity of the maser. In practice, an intensity per velocity channel is generated, which is then scaled by the total number of position pixels spanned by the beam to yield the intensity per channel per position pixel. This brings us to the next step, which is to construct a cube domain in which the masers can be placed in as described by their corresponding 3D Gaussian.

There are two important criteria to consider when constructing the cube domain. First, the channel spacing in each axis must satisfy the Nyquist Theorem to prevent aliasing errors. In the case of the position axes, an additional condition is that the boundaries must be wide enough to fully represent the beam shape. Then, the second criterion is that the size of the cube must be computationally feasible. This turns out to be a surprisingly strong condition, in particular due to the wide velocity range and narrow line width of the maser features: $v_{red,max} - v_{blue,min} \cong 2000 km/s$, $\delta v \cong 2km/s$. For these reasons, we decide on a position axis channel spacing of 1/5 of the narrower beam width, and a velocity axis channel spacing of half of the line width. This results in roughly 2×10^7 vertex points to calculate per maser feature. Fortunately, this computation time can be improved exponentially by creating a meshgrid of the 3D coordinates, contrary to iterating through three nested loops that are the x axis, y axis, and v axis.

3.2 Creating the Noise Cube

Once the signal cube is created, the next step is to reconstruct the random observational noise present in VLBI images. To accomplish this, for each velocity channel, we generate Gaussian random noise in each position pixel and convolve the image with the beam shape. Here, similar to the issue of A as discussed in the previous section, it is important to scale the Gaussian noise by the number of pixels covered by the beam. This is crucial in scaling the noise and signal cubes to the desired ratio later on. In addition, for consistency, the noise cube domain is created to have the exact same dimensions as the signal cube. To convolve the random noise with the beam, we take the Fourier transform of the Gaussian noise image and the beam

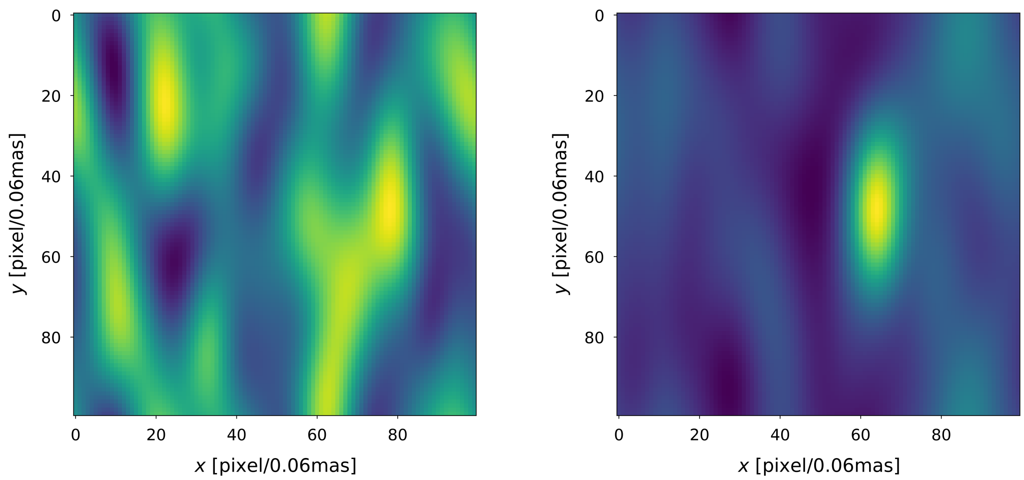

(a) (b)

Figure 3.1: (a) A velocity channel slice of the beam convolved noise cube. (b) A single maser signal added to beam convolved noise.

shape, multiply them element-wise in the Fourier space, and inverse Fourier transform the resulting image back to position space. This is mathematically equivalent to convolving the Gaussian noise image with the beam[1], but computationally much faster as it relies on parallel computation rather than a serial convolution algorithm. Figure 3.1(b) shows the resulting beam-convolved gaussian noise added to a signal.

Once the noise cube is generated, the next step is to add the noise cube to the signal cube, thus creating the science cube. By integrating over all positions, we can obtain a spectrum that can be visually compared to observed spectra, as shown in figure 3.3. By integrating over all velocity channels, we can also obtain a map of the maser disk, as displayed in figure 3.2.

3.3 Beam-Fitting the Cube

The science cube created from the method outlined above can now be processed exactly the same as a real VLBI data set. For each velocity channel, a 2 dimensional Gaussian is fit to the position map with the amplitude and central position as the free parameters. The standard deviation in each axis is fixed such that the fitting function matches the beam shape. Once the fitting is performed for all velocity channels, a maximum χ^2 threshold is imposed to remove the low-quality fits that do not represent an actual maser signal. Any fit that passes this threshold corresponds to a maser

[1]The convolution theorem.

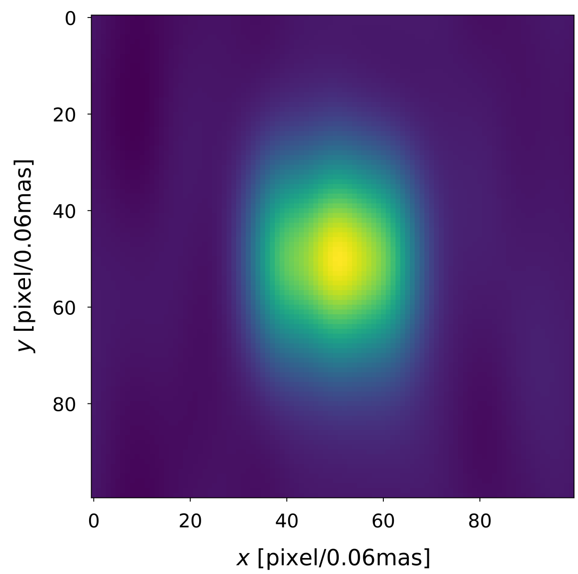

Figure 3.2: Position map of 40 maser features integrated over velocity.

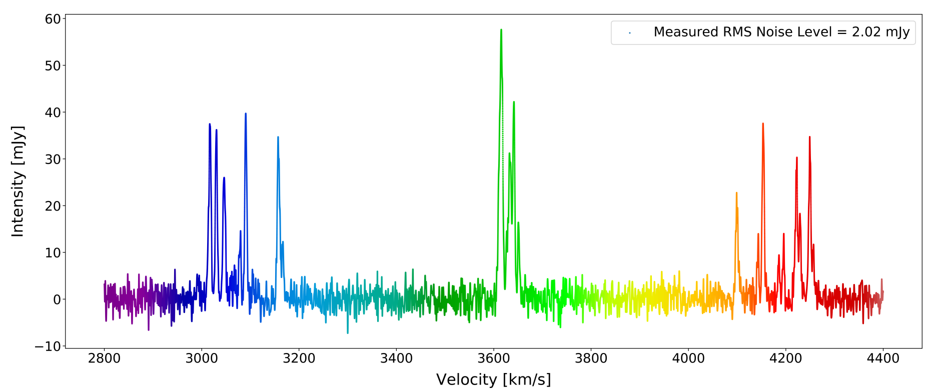

Figure 3.3: Velocity spectrum of figure 3.2 with 2mJy noise per 1km/s channel.

detection. Finally, the fitted amplitude is divided by the measured RMS noise level per velocity channel to obtain the signal-to-noise ratio for each maser detection. The SNR is then used to estimate the uncertainty in position measurement as described in equation 3.2.

$$\sigma_i = \frac{b_i}{2 \times \mathrm{SNR}} \qquad (i = x, y) \tag{3.2}$$

Chapter 4

Analysis

4.1 Spanning the Observational Error Space

As stated in the Introduction, the main goal of the MCP is to narrow the error constraint on the Hubble constant down to a few percent. This constraint is determined from the a posteriori uncertainties from the MCP fitting code, which inevitably depend on the a priori uncertainties that are the observational errors. The MCP strategy depends on two independent measurements, i.e. VLBI observations and single-dish spectral monitoring, meaning that there are two independent observational errors that we can improve on. The first improvement is to reduce the RMS noise in the VLBI map, which would reduce the uncertainty in the masers' positions. This improvement could be achieved, for example, by increasing the VLBI observing time to enhance the signal to noise ratio. Independently, the acceleration uncertainties could also be reduced to achieve our target total uncertainty on the Hubble constant, and we must allocate finite resources to the two areas of improvement. Thus, an understanding of how the a posteriori uncertainties depend on observational errors is critical in optimizing observations.

The simulation process presented in this thesis provides an effective method to explore the relationship between input observational error and the a posteriori error from the fitting code. By simply adjusting the noise cube as described in Chapter 3, we are free to set the mapping noise to the desired level while fixing or changing the nominal acceleration uncertainty.

For the purpose of spanning the observational error space, we adopt the 2D fitting code used by Braatz et al.[2] instead of the full 3D MCMC fitting code. This substitution saves computation time, allowing us to explore a greater range of error space. The main difference from the 3D fitting code is that the 2D fitting code assumes a "single-ring" model: the systemic masers originate from a single radius in the accretion disk, which is not uncommon for real galaxies. This feature can be observationally inferred from the position-velocity (PV) diagram as illustrated in figure 4.1(a). By extending the systemic line (marked green) in the PV diagram along its slope, we can connect the line to the high velocity curves; the two points of contact show the angular size of the ring from which the systemic features originate, and also the rotational velocity of this ring.

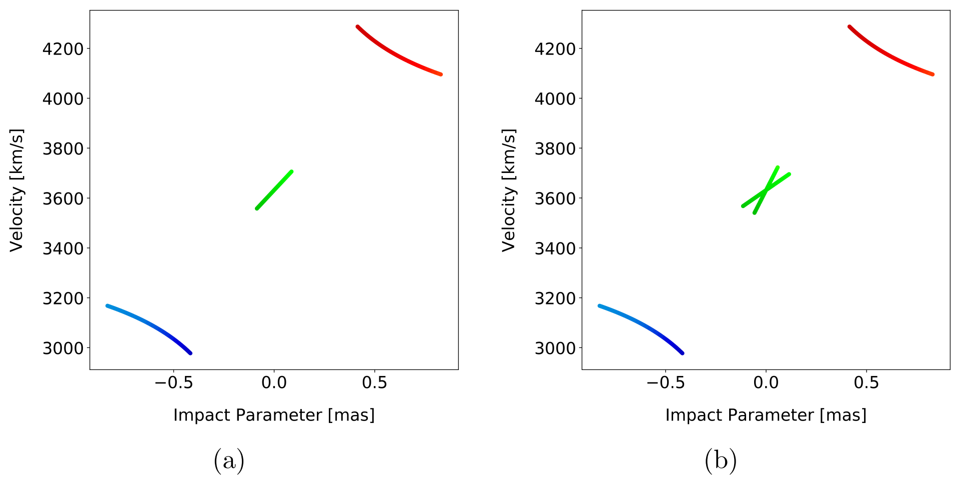

Figure 4.1: (a) Position-velocity (PV) diagram for a single-ring maser disk. (b) PV diagram for a two-ring maser disk as a comparison. Each slope originates from a different ring radius.

Based on the observational uncertainties reported by Braatz et al. [2], we span the error space from $(\delta\nu, \delta A) = (0.2\text{mJy}, 0.05\text{km/s/yr})$ to $(2.0\text{mJy}, 0.25\text{km/s/yr})$, where $\delta\nu$ represents the noise level per channel and δA is the uncertainty in acceleration. The nominal value $(\delta\nu, \delta A) = (1.5\text{mJy}, 0.2\text{km/s/yr})$ is used as the current position of the MCP in error space. A simulated data set from this error value yields an a posteriori distance uncertainty of 14%.

Figures 4.2, 4.3(a), and 4.3(b) summarize the results from this analysis from which we can draw a number of notable conclusions. For example, suppose that our goal is to reduce the distance uncertainty to 10% for a single galaxy[1] from the current value of 14%. How much improvement is required in either $\delta\nu$ or δA to achieve this goal? Following the δA isocurve in figure 4.3(a), down from the current point marked in green, we see that even at 0.25 mJy, which is 6 times lower than the current value, δD remains at approximately 12%. On the other hand, following the $\delta\nu$ isocurve in figure 4.3(b), a factor of 4 improvement in δA lowers δD down to approximately

[1]The total uncertainty on MCP distance measurements scale by the square root of the number of galaxies observed

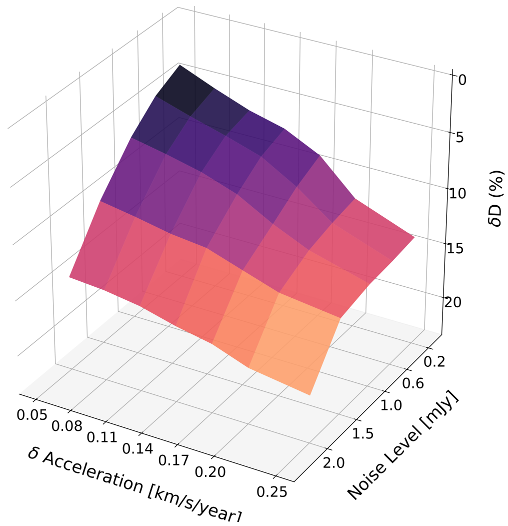

Figure 4.2: Various a posteriori uncertainties in distance generated from different points in the observational error space. The z-axis has been inverted, so the highest point indicates the lowest error in distance.

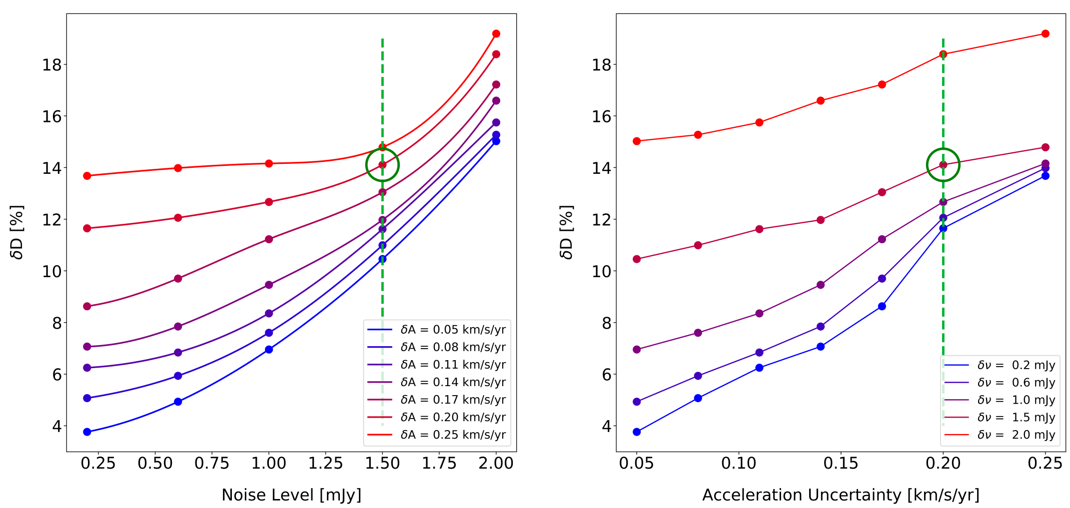

(a) (b)

Figure 4.3: (a) RMS Noise cross-section of figure 4.2. (b) δA cross-section of figure 4.2. Green indicates the current uncertainty level in both plots.

10%. Thus, future observing strategies should be focused on improving δA in order to achieve a lower δD. A similar point can be made by observing the overall scatter in the y axis in figures 4.3(a) and 4.3(b). While the former shows a clear widening in δD as the x axis decreases, the latter shows a less dramatic change. Thus, for improvements in $\delta\nu$ to take greater effect on δD, δA must be reduced first to a lower isocurve in figure 4.3(a).

4.2 Future Projects

Exploring the a priori uncertainty space is only one of many projects that can be accomplished with simulated data sets. For example, the method described in the previous section can easily be applied to other parameter spaces such as the warping parameter, number of maser features, black hole mass, and even the distance to the galaxy. Understanding the role of such parameters in determining the a posteriori distance uncertainty would provide an invaluable tool to maximize the efficiency in allocating MCP resources.

Independent of optimizing observations, another important component of the MCP method that can be thoroughly studied with simulated data sets is the 3D MCMC fitting code. For example, different MC sampling algorithms can show distinct converging characteristics in both efficiency and effectiveness. In terms of efficiency, the convergence times of different algorithms can be compared; in terms of effectiveness, we can examine the issue of the fitting code reporting undesired local minima as the converged estimate.

Chapter 5

Conclusion and Summary

In this thesis, we presented a method to simulate data sets of maser hosting accretion disks for the Megamaser Cosmology Project. This method could be broken down into two steps, the first of which is to simulate the disk itself, and the second step to simulate the observation of the disk. In simulating the disk, we made an assumption that the gravity of the central black hole would dominate the disk dynamics to first order, which is also seen in observations of actual maser galaxies. In addition, the intensities of individual masers were randomly sampled from an exponential distribution to reflect the stochastic nature of maser amplification, under an envelope defined by the maximum gain path set by the disk geometry and velocity coherence. Once all of the physical properties of the disk had been generated, we constructed a data cube with two positional axes and one velocity axis to contain the disk. To incorporate noise in VLBI mapping, we added a beam-convolved Gaussian noise to the data cube. From this point on, we could process the data cube with the same tools used in real MCP observations, and thus produce a simulated data set for the fitting code.

As an immediate application of the simulated data, we investigated the relationship between the a priori uncertainties in the fitting code and the a posteriori distance uncertainty. In particular, we spanned the observational uncertainty space in δA, the acceleration uncertainty, and $\delta\nu$, the VLBI mapping noise. As expected, a decrease in either uncertainty led to a monotonic decrease in the a posteriori distance uncertainty. The vertex in the error space with lowest uncertainty, $(\delta A, \delta\nu) = (0.05\text{km/s/yr}, 0.2\text{mJy})$, yielded a distance error of 4%. A more interesting conclusion could be drawn from comparing the gradient in each axis from the current uncertainty level of the MCP, defined by the observations of UGC 3789, at $(\delta A, \delta\nu) = (0.2\text{km/s/yr}, 1.5\text{mJy})$ and $\delta D = 14\%$. A steeper decrease in distance uncertainty for the δA axis was observed; in particular, to obtain the benchmark distance uncertainty of 10%, a δA improvement to 0.05km/s/yr was enough, while $\delta\nu$ required an improvement beyond the error range that we explored in this thesis. Thus, we concluded that a strategic improvement of the acceleration measurements would greater benefit the MCP than reducing the VLBI mapping noise.

Bibliography

[1] V. Bonvin, F. Courbin, S. H. Suyu, P. J. Marshall, C. E. Rusu, D. Sluse, M. Tewes, K. C. Wong, T. Collett, C. D. Fassnacht, T. Treu, M. W. Auger, S. Hilbert, L. V. E. Koopmans, G. Meylan, N. Rumbaugh, A. Sonnenfeld, and C. Spiniello. H0licow – v. new COSMOGRAIL time delays of HE 0435-1223:h0to 3.8 per cent precision from strong lensing in a flat {*upLambda*CDM model. *Monthly Notices of the Royal Astronomical Society*, 465(4):4914–4930, nov 2016.

[2] J. A. Braatz, M. J. Reid, E. M. L. Humphreys, C. Henkel, J. J. Condon, and K.Y. Lo. THE MEGAMASER COSMOLOGY PROJECT. II. THE ANGULAR-DIAMETER DISTANCE TO UGC 3789. *The Astrophysical Journal*, 718(2):657–665, jul 2010.

[3] Planck Collaboration. Planck intermediate results. *Astronomy & Astrophysics*, 596:A107, dec 2016.

[4] F. Gao, J. A. Braatz, M. J. Reid, K. Y. Lo, J. J. Condon, C. Henkel, C. Y. Kuo, C. M. V. Impellizzeri, D. W. Pesce, and W. Zhao. THE MEGAMASER COSMOLOGY PROJECT. VIII. a GEOMETRIC DISTANCE TO NGC 5765b. *The Astrophysical Journal*, 817(2):128, jan 2016.

[5] J. E. Greene, A. Seth, M. Kim, R. Läsker, A. Goulding, F. Gao, J. A. Braatz, C. Henkel, J. Condon, K. Y. Lo, and W. Zhao. MEGAMASER DISKS REVEAL a BROAD DISTRIBUTION OF BLACK HOLE MASS IN SPIRAL GALAXIES. *The Astrophysical Journal*, 826(2):L32, jul 2016.

[6] C. Y. Kuo, J. A. Braatz, K. Y. Lo, M. J. Reid, S. H. Suyu, D. W. Pesce, J. J. Condon, C. Henkel, and C. M. V. Impellizzeri. THE MEGAMASER COSMOLOGY PROJECT. VI. OBSERVATIONS OF NGC 6323. *The Astrophysical Journal*, 800(1):26, feb 2015.

[7] C. Y. Kuo, J. A. Braatz, M. J. Reid, K. Y. Lo, J. J. Condon, C. M. V. Impellizzeri, and C. Henkel. THE MEGAMASER COSMOLOGY PROJECT. v. AN ANGULAR-DIAMETER DISTANCE TO NGC 6264 AT 140 mpc. *The Astrophysical Journal*, 767(2):155, apr 2013.

[8] M. J. Reid, J. A. Braatz, J. J. Condon, L. J. Greenhill, C. Henkel, and K. Y. Lo. The megamaser cosmology project. i. very long baseline interferometric observations of UGC 3789. *The Astrophysical Journal*, 695(1):287–291, mar 2009.

[9] M. J. Reid, J. A. Braatz, J. J. Condon, K. Y. Lo, C. Y. Kuo, C. M. V. Impellizzeri, and C. Henkel. THE MEGAMASER COSMOLOGY PROJECT. IV. a DIRECT MEASUREMENT OF THE HUBBLE CONSTANT FROM UGC 3789. *The Astrophysical Journal*, 767(2):154, apr 2013.

[10] Adam G. Riess, Lucas M. Macri, Samantha L. Hoffmann, Dan Scolnic, Stefano Casertano, Alexei V. Filippenko, Brad E. Tucker, Mark J. Reid, David O. Jones, Jeffrey M. Silverman, Ryan Chornock, Peter Challis, Wenlong Yuan, Peter J. Brown, and Ryan J. Foley. A 2.4% DETERMINATION OF THE LOCAL VALUE OF THE HUBBLE CONSTANT. *The Astrophysical Journal*, 826(1):56, jul 2016.